ACS OMEGA

http://pubs.acs.org/journal/acsodf

Article

A Model for Radiolysis in a Flowing-Water Target during High-Intensity Proton Irradiation

Katharina A. Domnanich* and Gregory W. Severin

Cite This: *ACS Omega* 2022, 7, 25860−25873

Read Online

ACCESS | Metrics & More | Article Recommendations | Supporting Information

ABSTRACT: At the Facility for Rare Isotope Beams (FRIB), interactions between heavy-ion beams and beam-dump water will create a wide variety of radionuclides which can be accessed by a technique known as "isotope harvesting". However, irradiation of water is always accompanied by the creation of numerous radical, ionic, and molecular radiolysis products. Some of the radiolysis products have sufficiently long lifetimes to accumulate in the irradiated water and affect the harvesting chemistry. Here we investigate the formation of hydrogen peroxide, molecular hydrogen, and molecular oxygen during a high-intensity proton irradiation of a flowing-water isotope-harvesting target and compare the experimental results to simulations. The simulations kinetically model the chemical reactions occurring in the homogeneous phase of radiolysis in flowing water and establish an "effective yield". In both the experiment and simulations, the bulk quantities of H_2, H_2O_2, and O_2 are considerably lower than predicted by primary radiolysis yields (escape yields), meaning that in the high beam intensity regime the homogeneous phase reactions have a considerable impact on the overall chemical composition of the water. Further, it could be shown that for radiation which is characterized by a limited linear energy transfer, such as the here applied protons, the bulk outcome of the microscopic kinetic modeling could be estimated by a simplified steady-state model.

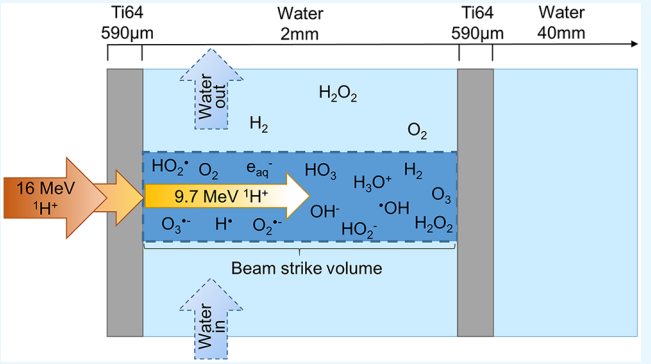

1. INTRODUCTION

The Facility for Rare Isotope Beams (FRIB) will create beams of radionuclides that have previously only existed in extreme cosmic environments. With its commissioning in 2022, FRIB will allow researchers to address forefront scientific questions in nuclear science. In the background of FRIB's fundamental science efforts, there is an opportunity to use the high-energy ion beams to create additional radionuclides in the FRIB beam dump. The FRIB beam dump is a spinning drum of Ti64 alloy (6% Al, 4% V, balance Ti) which is continuously traversed by a stream of cooling water.[1,2] With a heavy-ion beam impinging on the nuclei of water molecules, nuclear reactions are induced, resulting in the formation of a variety of different radionuclides. In this way, a yet unexploited source of rare radionuclides becomes accessible and contributes to meeting the increasing demands of medicine, astrophysics, materials science, and stockpile stewardship science. So far exploratory research with the heavy-ion beams from the National Superconducting Cyclotron Laboratory (NSCL) has been conducted and facilitated the collection of various radioactive species, such as ^{24}Na, ^{47}Ca, ^{48}V, ^{62}Zn, ^{67}Cu, $^{76/77}$Kr, and ^{88}Zr.[2−11]

The slowing down of heavy ions when passing through water is mediated by inelastic collisions with bound electrons. The energy loss per unit distance, expressed as stopping power, determines the structure of ionization tracks and their relatively short ranges.[12,13] Following the initial energy deposition and ionization events, HO−H bond breaking occurs, and the decomposition of water molecules is initiated. The resulting species (OH, H, H_3O^+ and e^-_{aq}) are non-homogeneously distributed in separated regions, also known as "spurs", along the radiation track. The track expands as these initial species react within the spur, forming the primary radiolysis species e^-_{aq}, OH, H, HO_2, H_3O^+, OH^-, H_2O_2, and H_2. All recombination and spur expansion processes are completed ∼1 μs after the initial energy deposition. The molecular and radical species present at that time are defined by the primary radiolytic yield (also known as G value or escape yield) and are usually expressed as the number of molecules created per 100 eV of deposited energy.[14−16] Escape yields in a medium are determined by the prevailing track structure which is heavily dependent on the radiation type and energy. The heavy ions' linear energy transfer (LET), which is

Received: June 6, 2022
Accepted: June 23, 2022
Published: July 12, 2022

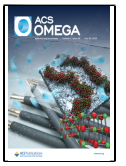

© 2022 The Authors. Published by American Chemical Society

assumed to be equivalent to the stopping power in liquid water, is commonly used to describe the spatial distribution of the tracks.[17,18] The formation of the spurs is followed by diffusion of the species into the bulk solution, where they react with each other and with the surrounding molecules in the solvent. Within this chemistry stage, the system evolves via homogeneous kinetics where secondary products, among them O_2, are formed. The homogeneous reactions determine the temporal development of the concentrations of primary radiolysis species.[16,19,20] In closed systems exposed to low-LET irradiations over extended time periods, a chemical equilibrium will be established between the formation and removal processes. Such steady-state conditions stabilize the concentrations of radiolytic species on a moderate level, prevailing as long as the irradiation conditions are stable.[20,21] However, with high-LET radiation, water molecules will be decomposed continuously, and the establishment of a steady state is not expected.[13,22]

For the irradiation of more complex systems, mass transport to nonirradiated volumes needs to be taken into consideration. Radicals generally react away quickly once they leave the irradiated zone, while the lifetimes of molecular products are sufficiently long to allow an accumulation and to affect the radiolysis environment of the water.[21,23] The most recent exploratory isotope harvesting studies at the NSCL were performed with a water-traversed beam blocker manufactured from Ti64-alloy, which mimics the conditions expected at FRIB. The radionuclides were created in the water matrix and transported to the collection sites by the continuous circulation of a large water volume (~40 L). Depending on the volatility of the respective species, the collection is accomplished either from the aqueous phase on ion exchange resins or on gas traps after a carrier gas stream transferred the gaseous radionuclides into the headspace.[4] In addition to acquiring the necessary technical and chemical knowledge about the isotope harvesting process, the suitability of the Ti64-alloy shell material was assessed. This was realized by high-intensity proton irradiation at the University of Wisconsin-Madison Cyclotron Laboratory (UW).[24]

In consideration of our isotope harvesting efforts, additional importance is attached to understanding water conditions and the effects of radiolysis. A prediction of the expected concentrations of H_2, H_2O_2, and O_2 with an escape yield-based model was regarded as valid when taking the large volume of irradiated water into account. However, increasing discrepancies between the predicted and observed levels were recognized at elevated beam currents. The escape yields reported in the literature suggest a beam current independent behavior in the intensity range of a few nanoampere.[19] Given that the focus of our experiments is directed toward the generation of radionuclides, the applied beam intensities were several orders of magnitude higher. Based on our observations, substantial interactions of all radiolytic species inside the irradiated volume are presumed.

In this work, an in-house written Python code was used to simulate the radiolysis reactions inside the flowing-water target during the proton irradiation. The computations suggest a dependence of the observed yields on the applied beam currents as well as on the prevailing concentrations of molecular hydrogen, hydrogen peroxide, and oxygen. However, the significance of the effective yield estimation was demonstrated to be less important once the concentrations within the entire system's water approach steady-state conditions. While the establishment of a steady state is known to occur when low-LET radiation is applied onto unified water volumes, the contrast to our system is that our system consists of a small, beam-irradiated chamber, connected to a large, nonirradiated volume. However, at FRIB, predominantly heavy-ion beams of high LET will be studied. Under such conditions, the formation of molecular products is believed to follow an effective yield-based model, rather than transitioning toward a steady state. This radiolysis model establishes the groundwork for a later translation toward the conditions at FRIB and will aid in estimating the levels of radiolysis products generated during isotope harvesting.

2. MATERIALS AND METHODS

2.1. Isotope Harvesting System and Experimental Setup. The proton irradiation was conducted at the UW (University of Wisconsin) Medical Physics Department's GE PETtrace cyclotron and focused on the assessment of the durability of the flowing-water isotope harvesting target. An exhaustive description of the experimental design as well as the results of the study are published in a separate publication.[24] While the preliminary results on radiolysis are described there as well, the underlying radiolysis mechanisms were not discussed, and no in-depth explanations about the observed phenomena were provided. To move ahead, simulation was viewed as a useful tool for unraveling the details of the bulk radiolysis yields.

Here, a brief overview of the experimental setup is given to enhance the understanding of the simulation. The proton beam was extracted from the cyclotron with an energy of 16 MeV and was directed toward the water-filled beam blocker. Due to geometrical constraints, it was not possible to measure a suppressed beam current. Therefore, the beam intensity was inferred by combining information from calibrated and suppressed Faraday cups upstream of the beam blocker with the unsuppressed current. In addition, the beam current was benchmarked against the induced radioactivity in the beam blocker window. The entire irradiation (~3.3 h) was divided into four irradiation periods, where the beam current was ramped up steadily, resulting in intensities of 1−33.7 μA.

The beam blocker is manufactured from 3D-printed titanium alloy (Ti64, 90% Ti, 6% Al, 4% V, Stratasys, Minneapolis MN, USA) and encompasses integrated channels to establish water flow. After passing through the 590 μm thick Ti64 front face, the proton energy was degraded to 9.7 MeV. A detailed description of the beam blocker is given elsewhere.[4] An overview of the isotope harvesting system is provided by the schematic diagram in the Supporting Information, Figure S1, while the passage of the proton beam through the target is depicted in the Supporting Information, Figure S2.

With the low-energy proton beam impinging on the water-filled beam blocker, the induced nuclear reactions are limited to fusion-evaporation in the water and the target shell. The created radionuclides, such as ^{13}N, ^{18}F, ^{48}V, and ^{51}Cr, were transported away from the production site by the fast water flow (13.2 L/min) through the target, also referred to as the "main loop". This main loop is interfaced with the harvesting system, consisting of a reservoir of around 36 L of water. To facilitate the circulation of water, the pump operated in a constant pressure mode, set to 45 psi. Radionuclides were extracted from the water with ion exchange resins, while volatile species were captured from the gas phase on a variety

https://doi.org/10.1021/acsomega.2c03540
ACS Omega 2022, 7, 25860−25873

of traps. These processes are organized in several subunits off the main loop.[24]

The concentrations of radiolytic hydrogen, hydrogen peroxide, and oxygen were monitored throughout the irradiation. An online assessment of the H_2 and O_2 levels was achieved with one hydrogen sensor and two dissolved oxygen sensors (referred to later as "sensor 1" and "sensor 2"). A stream of He purge gas passing through the water reservoir facilitated the transportation of gaseous radionuclides from the system's water to their collection sites, as well as the removal of dissolved oxygen and hydrogen. During temporary suspensions of the irradiation, water samples of ∼50 mL were withdrawn and analyzed for the hydrogen peroxide content. The quantification was accomplished by a semiquantitative strip test immediately after removal of the sample and by a precise spectrophotometric analysis, done within 7 days after the experiment.[4] To prevent an accumulation of H_2O_2 to levels which could adversely affect the equipment, a subunit accommodated a H_2O_2 disintegration system. The catalytic reaction, which is mediated by the noble metals Pt and Pd, follows the overall reaction: $H_2O_2 \rightarrow H_2O + {}^1/_2O_2$.[25] Additionally, a heat exchanger connected to a chiller was employed to maintain the water temperature at ∼25 °C. Considering the low levels of generated radioactive species and the low observed conductivity, the pH of neutral water was estimated for this experiment.

2.2. Radiolysis Measurements and System Conditions. The concentrations of radiolytically formed H_2, H_2O_2, and O_2 were predicted by mass transport calculations that are based upon production rates of the molecules in water and their simultaneous decomposition and volatilization rates. The dissolved gas equilibria were presumed to follow Henry's law. The extremely low concentrations of radioactive and stable components in the water render any solution composition effects negligible, and thus, Henry's law was considered as an adequate approximation. Further, Henry's law was applied in a previous study to describe the behavior of gaseous radionuclides in our isotope harvesting system, and the approximation was corroborated by the simultaneous measurement of the volatile species in the gas and water phase.[11]

The equations for estimating the levels of H_2, H_2O_2, and O_2 were published previously;[24] however, a brief overview of the computation is given in the Supporting Information, "Estimation of the H_2, H_2O_2, and O_2 levels". In brief, the levels of H_2 are predicted by assuming a beam power-dependent production rate and a concurrent exchange of H_2 between the water and its headspace. To determine the H_2 levels at the end of the gas loop, the H_2 produced in the water passes through the headspace and the traps before it is analyzed by the sensor (%H_2 at sensor). The equations for all the steps are outlined in the Supporting Information, eqs S1−S4. Similarly, the net balance of H_2O_2 is governed by a beam-induced formation and a continuous peroxide decomposition by the catalytic converter after the third irradiation period (Supporting Information, eq S5). The amount of dissolved oxygen in the system's water is approximated by a beam power-dependent production, a constant deaeration from the water, and additional O_2 input from the H_2O_2 decomposition when water is passed through the catalytic converter (Supporting Information, eq S6).[24]

The production rates are also known as escape yields or G values and are expressed in units of molecules/100 eV. Previously, a model developed by La Verne, in which the escape yield is expressed as a function of the parameter MZ^2/E, was used to predict the G values for H_2, H_2O_2, and O_2.[17,24] However, for light and low energetic ions the difference to the conventional LET model is negligible and in order to be consistent with all other literature data, the G values specified by Pastina et al. were used for computing the radiolysis product formation rates.[19]

2.3. Model Definition. The radiolysis model was developed in Python and refers to the homogeneous stage of radiolysis, which starts about 10^{-7} s after the deposition of ionizing radiation. At this time, the radiolytic products have already diffused away from the tracks and are uniformly distributed in the bulk solution. The radiolysis kinetics of this phase can be accurately described by the set of elementary chemical reactions given in Table 2.[19,26]

Simulation Model for a Closed Container. The first scenario for simulation involved numerically computing the saturation concentrations of radiolytic compounds during prolonged irradiation of water in a closed container. The model was designed to reproduce the conditions that would be reached when a 20 mL closed volume of water was uniformly exposed to either proton or γ radiation. For the ${}^1H^+$ irradiation model, a particle energy of 9.7 MeV was used, and an initial LET of 12.8 eV/nm was estimated with the Stopping and Range of Ions in Matter compilation code (SRIM 2013).[27] The simulations were performed with varying beam currents, ranging from 0.1 to 50 μA. The dose rates were calculated by considering the beam power deposited into the water volume. For the γ-radiolysis model, the dose rate was set to 0.25 Gy/s. Both scenarios ignored surface interactions and were treated as being perpetually homogeneous.

Inside the water volume the formation of the radiolytic species e_{aq}^-, H, H_2, OH, H_2O_2, HO_2, H^+, and OH^- is assumed to occur with the respective escape yields, given in Table 1.

Table 1. G Values Used in the Model Calculations (Units in Molecules/100 eV)[19]

species	G (10 MeV ${}^1H^+$)	G (γ-rays)
e^-_{aq}	0.90	2.60
H	0.57	0.66
H_2	0.64	0.45
OH	1.18	2.70
H_2O_2	0.74	0.70
HO_2	0.03	0.02
H^+	1.10	3.10
OH^-	0.20	0.50

The escape yields were published by Pastina et al. for γ-rays and 10 MeV ${}^1H^+$, where the latter is assumed to be a close approximation for the 9.7 MeV protons of the current experiment. With each delivered beam particle, the formation of primary radiolytic species is induced, and they are allowed to react homogeneously according to a set of 73 chemical reactions (Table 2). The reaction system was previously developed by Elliot et al. and successfully applied by Pastina et al. and Iwamatsu et al.[19,23,28] The simulation considers a constant temperature of 25 °C, and the pH of neutral water is accepted as an initial condition. During the chemistry phase numerous secondary species, such as HO_2^-, O_2^-, O_2, O^-, O_3^-, O_3, and HO_3 are created, and all begin to interact. Most of the elementary reactions are binary and have the general form

https://doi.org/10.1021/acsomega.2c03540
ACS Omega 2022, 7, 25860−25873

Table 2. Reactions and Rate Constants Used in the Simulation Models for the Closed Container and the Flowing-Water Target[a]

reaction no.	reaction	rate constant (M^{-1} s^{-1} or s^{-1})[b]
	Acid–Base Reactions	
0	$H^+ + OH^- \rightarrow H_2O$	1.18×10^{11} *
1	$H_2O \rightarrow H^+ + OH^-$	2.12×10^{-5} *
2	$H_2O_2 \rightarrow H^+ + HO_2^-$	9.43×10^{-2} *
3	$H^+ + HO_2^- \rightarrow H_2O_2$	5.02×10^{10} *
4	$H_2O_2 + OH^- \rightarrow HO_2^- + H_2O$	1.33×10^{10} *
5	$HO_2^- + H_2O \rightarrow H_2O_2 + OH^-$	1.27×10^{6} *
6	$e^-_{aq} + H_2O \rightarrow H + OH^-$	15.75 *
7	$H + OH^- \rightarrow e^-_{aq} + H_2O$	2.44×10^{7} *
8	$H \rightarrow e^-_{aq} + H^+$	5.83 *
9	$e^-_{aq} + H^+ \rightarrow H$	2.09×10^{10} *
10	$OH + OH^- \rightarrow O^- + H_2O$	1.33×10^{10} *
11	$O^- + H_2O \rightarrow OH + OH^-$	1.27×10^{6} *
12	$OH \rightarrow O^- + H^+$	9.43×10^{-2} *
13	$O^- + H^+ \rightarrow OH$	5.02×10^{10} *
14	$HO_2 \rightarrow O_2^- + H^+$	7.73×10^{5} *
15	$O_2^- + H^+ \rightarrow HO_2$	5.02×10^{10} *
16	$HO_2 + OH^- \rightarrow O_2^- + H_2O$	1.33×10^{10} *
17	$O_2^- + H_2O \rightarrow HO_2 + OH^-$	1.55×10^{-1} *
	Chemical Reactions	
18	$e^-_{aq} + OH \rightarrow OH^-$	3.55×10^{10} *
19	$e^-_{aq} + H_2O_2 \rightarrow OH + OH^-$	1.36×10^{10} *
20	$e^-_{aq} + O_2^- + H_2O \rightarrow HO_2^- + OH^-$	1.30×10^{10}
21	$e^-_{aq} + HO_2 \rightarrow HO_2^-$	1.30×10^{10} *
22	$e^-_{aq} + O_2 \rightarrow O_2^-$	2.29×10^{10} *
23	$2e^-_{aq} + 2H_2O \rightarrow H_2 + 2OH^-$	7.26×10^{9} *
24	$e^-_{aq} + H + H_2O \rightarrow H_2 + OH^-$	2.76×10^{10} *
25	$e^-_{aq} + HO_2^- \rightarrow O^- + OH^-$	3.50×10^{9}
26	$e^-_{aq} + O^- + H_2O \rightarrow 2OH^-$	2.20×10^{10}
27	$e^-_{aq} + O_3^- + H_2O \rightarrow O_2 + 2OH^-$	1.60×10^{10}
28	$e^-_{aq} + O_3 \rightarrow O_3^-$	3.60×10^{10}
29	$H + H_2O \rightarrow H_2 + OH$	4.58×10^{-5} *
30	$H + O^- \rightarrow OH^-$	1.00×10^{10}
31	$H + HO_2^- \rightarrow OH + OH^-$	9.00×10^{7}
32	$H + O_3^- \rightarrow OH^- + O_2$	1.00×10^{10}
33	$H + H \rightarrow H_2$	5.14×10^{9} *
34	$H + OH \rightarrow H_2O$	1.09×10^{10} *
35	$H + H_2O_2 \rightarrow OH + H_2O$	3.65×10^{7} *
36	$H + O_2 \rightarrow HO_2$	1.31×10^{10} *
37	$H + HO_2 \rightarrow H_2O_2$	1.14×10^{10} *
38	$H + O_2^- \rightarrow HO_2^-$	1.14×10^{10} *
39	$H + O_3 \rightarrow HO_3$	3.80×10^{10}
40	$OH + OH \rightarrow H_2O_2$	4.81×10^{9} *
41	$OH + HO_2 \rightarrow H_2O + O_2$	8.84×10^{9} *
	Chemical Reactions	
42	$OH + O_2^- \rightarrow OH^- + O_2$	1.10×10^{10} *
43	$OH + H_2 \rightarrow H + H_2O$	3.95×10^{7} *
44	$OH + H_2O_2 \rightarrow HO_2 + H_2O$	2.92×10^{7} *
45	$OH + O^- \rightarrow HO_2^-$	2.50×10^{10}
46	$OH + HO_2^- \rightarrow HO_2 + OH^-$	7.50×10^{9}
47	$OH + O_3^- \rightarrow O_3 + OH^-$	2.60×10^{9}
48	$OH + O_3^- \rightarrow 2O_2^- + H^+$	6.00×10^{9}
49	$OH + O_3 \rightarrow HO_2 + O_2$	1.10×10^{8}
50	$HO_2 + O_2^- \rightarrow HO_2^- + O_2$	8.00×10^{7}
51	$HO_2 + HO_2 \rightarrow H_2O_2 + O_2$	8.40×10^{5} *
52	$HO_2 + O^- \rightarrow O_2 + OH^-$	6.00×10^{9}
53	$HO_2 + H_2O_2 \rightarrow OH + O_2 + H_2O$	0.50
54	$HO_2 + HO_2^- \rightarrow OH + O_2 + OH^-$	0.50
55	$HO_2 + O_3^- \rightarrow 2O_2 + OH^-$	6.00×10^{9}
56	$HO_2 + O_3 \rightarrow HO_3 + O_2$	5.00×10^{8}
57	$2O_2^- + 2H_2O \rightarrow H_2O_2 + O_2 + 2OH^-$	0.3 *
58	$O_2^- + O^- + H_2O \rightarrow O_2 + 2OH^-$	6.00×10^{8}
59	$O_2^- + H_2O_2 \rightarrow OH + O_2 + OH^-$	0.13
60	$O_2^- + HO_2^- \rightarrow O^- + O_2 + OH^-$	0.13
61	$O_2^- + O_3^- + H_2O \rightarrow 2O_2 + 2OH^-$	1.00×10^{4}
62	$O_2^- + O_3 \rightarrow O_3^- + O_2$	1.50×10^{9}
63	$2O^- + H_2O \rightarrow HO_2^- + OH^-$	1.00×10^{9}
64	$O^- + O_2 \rightarrow O_3^-$	3.75×10^{9} *
65	$O^- + H_2 \rightarrow H + OH^-$	1.28×10^{8} *
66	$O^- + H_2O_2 \rightarrow O_2^- + H_2O$	5.00×10^{8}
67	$O^- + HO_2^- \rightarrow O_2^- + OH^-$	7.86×10^{8} *
68	$O^- + O_3^- \rightarrow 2O_2^-$	7.00×10^{8}
69	$O^- + O_3 \rightarrow O_2^- + O_2$	5.00×10^{9}
70	$O_3^- \rightarrow O_2 + O^-$	2.62×10^{3} *
71	$O_3^- + H^+ \rightarrow O_2 + OH$	9.00×10^{10}
72	$HO_3 \rightarrow O_2 + OH$	1.10×10^{5}

[a]The reactions and rate constants were taken from Pastina *et al.*[19] For the reactions where water is a reactant, Pastina *et al.* considered the concentration of water in the expression of the rate constant. However, in the present system pure water is the main component, while the concentrations of H_2, H_2O_2, and O_2 are in the μM range. Therefore, this term was considered negligible, and only the numerical expressions of the rate constants are given in the following table. [b]For several reactions updated rate constant data were available from Elliott & Bartels.[29] The data from this compilation were used to compute the reaction rate constants for a water temperature of 25 °C. Updated rate constants are labeled by an asterisk (*).

$$A + B \xrightarrow{k_{AB\rightarrow CD}} C + D$$

representing the reaction of species A and B to form species C and D with a rate constant $k_{AB\rightarrow CD}$. When following any given species C, it is consumed in reactions with the same form, for example,

$$C + E \xrightarrow{k_{CE\rightarrow FG}} F + G$$

representing the reaction of species C and E to form species F and G with a rate constant $k_{CE\rightarrow FG}$.

In the Python code, differential equations were used to describe this system of interactions and to compute the time-dependent concentrations. For example, the differential equation following the concentration of any radiolytic species, $[C]$, in the water is expressed generically by eq 1:

$$\frac{d[C]}{dt} = G_C \cdot I(t) + \sum_{A,B,E} \{k_{AB\rightarrow CD}[A][B] - k_{CE\rightarrow FG}[C][E]\} \quad (1)$$

where the first term, $G_C \cdot I(t)$, represents the beam-induced generation of species, and the following two terms account for the chemical reactions leading to the formation and destruction of species C as shown in reactions 1 and 2, respectively. Finally, the concentrations of all species were calculated through simultaneous numerical integration of the differential equations using one-nanosecond time steps.

https://doi.org/10.1021/acsomega.2c03540
ACS Omega 2022, 7, 25860−25873

A time resolution of one nanosecond was considered adequate to accurately estimate the levels of all radicals, ions, and molecules resulting from the complex interactions. However, the fast reaction rates of the interconversion between the protonated and deprotonated species, such as $H_2O \leftrightarrow H^+ + OH^-$ ($pK_a = 13.999$), $H_2O_2 \leftrightarrow H^+ + HO_2^-$ ($pK_a = 11.65$), $OH \leftrightarrow H^+ + O^-$ ($pK_a = 11.9$), and $HO_2 \leftrightarrow H^+ + O_2^-$ ($pK_a = 4.57$),[19] required additional consideration. The quantities of all protonated and deprotonated species formed in chemical reactions with their specific rate constants (i.e., for H_2O: rxn 0 and 1, for H_2O_2: rxn 2 and 3, for OH: rxn 12 and 13, for HO_2: rxn 14 and 15 in Table 2) were compared with the quantities resulting from an adjusted acid−base equilibrium. The smaller values were used to approximate the levels at the end of the respective time step.

Simulation Model for the Flowing-Water Target. In a further development, the model was adapted to recreate the conditions during the 9.7 MeV proton irradiation of the flowing water as closely as possible. Given that the entire beam power is deposited in the first water-traversed channel in the experimental beam blocker, the formation of all radiolytic species occurs in this region. Based on previous observations, the directly irradiated area is estimated to be 0.7 cm^2. The irradiated water volume (in the following referred to as "beam strike volume") is defined by the 2 mm distance between the two Ti64 sheets and amounts to 0.14 mL. The number of protons delivered by the applied beam currents, ranging from 1 to 33.7 μA, occurred at a frequency of 27.2 MHz and resulted in the transmission of 2.23×10^{12}−7.50×10^{13} eV per pulse. With each delivered beam pulse the formation of primary species is induced. Their formation and subsequent reactions are based on the same set of escape yields and chemical reactions as described previously for the closed container model.

The flowing-water target was traversed by a fast water flow of 220.8 mL/s, which resulted in a flow of 41.7 mL/s through the beam strike volume. Thus, all the produced radiolytic species are continuously transported away from the irradiation site. This scenario is considered in the model by introducing a constant supply of fresh solution into the beam spot volume (Figure 1) with the removal of an equivalent amount of irradiated solution. The water in the beam spot was assumed to be instantaneously, and perfectly mixed. The evolution of all molecular and radical species was followed until equilibrium was attained, which occurred after ∼20 ms in all evaluated conditions. The steady-state concentrations of H_2, H_2O_2, and O_2 were used to compute their effective production yields, also denoted as effective G values (G_{eff}). Over the entire irradiation time of the experiment (∼3.3 h), the extended lifetimes of the molecular species enabled an accumulation in the system's water. To recreate this behavior in the simulations, the solution inside the beam strike volume (in the following designated as "baseline" concentration), as well as the supplying solution, were assumed to encompass varying concentrations of H_2, H_2O_2, and O_2. This allowed us to assess the influence of different hydrogen, peroxide, and oxygen concentrations on the respective effective yields.

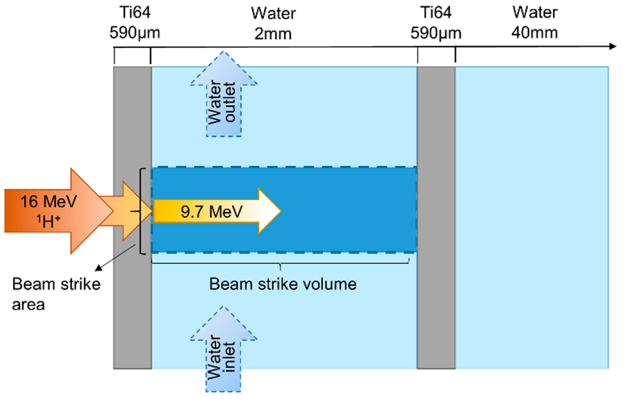

Figure 1. A 16 MeV proton beam passes through the first layer of Ti64, uniformly dispersed over an area of about 0.7 cm^2. At the interface of the water, the protons encompass an energy of 9.7 MeV which they dissipate entirely in the volume between the two Ti64 sheets. This "beam strike volume" amounts to 0.14 mL, and the locally generated radiolytic and nuclear species are continuously transported away by the fast water flow (41.7 mL/s).

2.4. Radiolysis Reactions in the Proton-Irradiated Flowing-Water Target. The extent of the H_2 and H_2O_2 yield suppression within the flowing-water target was evaluated by introducing the "percentage metric for total yield suppression", S_{total} (eq 2):

$$S_{total} = \left(1 - \frac{G_{eff}}{G_{lit}}\right) \times 100 \quad (2)$$

where G_{eff} represents the unsuppressed effective yield and G_{lit} is the published literature G value. In this representation, a positive value indicates the percentage suppression of the computed effective yield in comparison to the literature escape yield, whereas an enhanced yield is illustrated by a negative value.

The chemical reactions influencing the levels of H_2 and H_2O_2 in the flowing-water target were identified by consecutively suppressing individual reactions and comparing the resulting effective yields with the unsuppressed ones. The "percentage metric for yield suppression by Allen cycle rxn", S_{Allen}, was computed by eq 3:

$$S_{Allen} = \left(1 - \frac{G_{eff}}{G_{Allen=0}}\right) \times 100 \quad (3)$$

where $G_{Allen=0}$ represents the effective yield computed with suppressed Allen cycle reactions (Table 2, rxn 35 and 43). A close approximation of this value to S_{total} can be considered as a qualitative measure for the contribution of the Allen cycle reactions toward the observed suppression of H_2 and H_2O_2, respectively.

The "percentage metric for yield suppression by H_2O_2-mediating rxn", $S_{H2O2\ rxn}$, is given by eq 4:

$$S_{H_2O_2rxn} = \left(1 - \frac{G_{eff}}{G_{H_2O_2,rxn=0}}\right) \times 100 \quad (4)$$

For the calculation of $G_{H2O2,rxn}$, not only the Allen cycle reactions but also other H_2O_2 pathways, such as the reactions with hydrated electrons and hydroxyl radicals (Table 2, rxn 19, 35, 40, 43, 44), were suppressed. A value close to S_{total} underlines the significance of all before-mentioned reactions toward the observed suppressed H_2O_2 yield.

2.5. Quantification of Proton Beam-Induced Radiolysis in the System's Water. The "Design of Experiments" feature of the statistical software "Minitab" (Minitab LCC, product version 20.1.2) was used to determine the functional

https://doi.org/10.1021/acsomega.2c03540
ACS Omega 2022, 7, 25860−25873

dependencies of the effective G values of H_2, H_2O_2, and O_2 on their respective concentrations as well as on the beam current. This approach encompassed the software-supported proposal of a set of experimental conditions, used as input parameters for simulating the effective yields. This was followed by a functional analysis to establish an empirical model. To enhance the descriptive ability of the model, the beam current range was divided into four segments (0.5−7.5, 7.5−15.0, 15.0−24.5, and 24.5−34.0 μA) where the levels of H_2, H_2O_2, and O_2 were varied over a reasonable concentration range. The concentration ranges were chosen with respect to the observed levels during the irradiation experiment. After computing the effective G values with the suggested inputs of H_2, H_2O_2, and O_2 concentrations and beam currents, the functional dependencies were found with the "Response Surface" method. Next to linear, possible quadratic correlations could also be considered with this method. The recommended model was improved by consecutively removing the terms identified as statistically insignificant at a significance level α of 0.05. With the optimized regression equations for the effective H_2, H_2O_2, and O_2 yields, their levels could be mapped for the entire irradiation experiment. For the effective yield-based model the literature escape yields (G) in eqs S1, S5, and S6, outlined in the Supporting Information, were replaced by the values of the respective effective yields (G_{eff}).

In the simulations, when the water flow rate is set to zero (i.e., irradiation of a closed small-volume system), the concentrations of H_2 and H_2O_2 inside the target approach steady states. In the flowing-water system, given the small target volume and high-power deposition, it is feasible that during the time a small volume of water is passing through the beam strike area, it could approach a local steady state. The G_{eff} model can be augmented to respect the steady-state limit by introducing a throttle on the rate of change in concentration of H_2 and H_2O_2. In this model, called the G_{eff} + SS model, an introduced constraint limits the changes in H_2 and H_2O_2 concentrations ($\Delta[H_2O_{2,Geff}]$ or $\Delta[H_{2,Geff}]$) during any time step to being no larger in magnitude that could be achieved when approaching the zero-flow steady-state limit. Thereby, the concentration of H_2O_2 at time t_i ($[H_2O_2]_{ti}$) is obtained by numerical integration of the following piecewise equation (eq 5):

$$[H_2O_2]_{t_i} = \begin{cases} \Delta[H_2O_{2_{Geff}}] + [H_2O_2]_{t_{i-1}} & \text{if } \Delta[H_2O_{2_{G_{eff}}}] < \Delta[H_2O_{2_{SS}}] \\ \Delta[H_2O_{2_{SS}}] + [H_2O_2]_{t_{i-1}} & \text{if } \Delta[H_2O_{2_{G_{eff}}}] \geq \Delta[H_2O_{2_{SS}}] \end{cases} \quad (5)$$

To estimate the H_2 concentration at time t_i ($[H_2]_{ti}$), all H_2O_2 related expressions in eq 5 are replaced by the equivalent H_2 expressions. The individual components of eq 5, that is, the difference in H_2O_2 and H_2 levels for the steady-state approximation ($\Delta[H_2O_{2,SS}]$ or $\Delta[H_{2,SS}]$) and the G_{eff} model ($\Delta[H_2O_{2,Geff}$ or $\Delta[H_{2,Geff}]$) are illustrated by eqs 6−8.

The difference in H_2O_2 levels for the steady-state approximation ($\Delta[H_2O_{2,SS}]$) within a 100 s time interval is given by eq 6:

$$\Delta[H_2O_{2_{SS}}] = [H_2O_2]_{SS,segment}(1 - e^{-k_{SS}\cdot\Delta t}) - [H_2O_2]_{t_{i-1}}(1 - e^{-k_{SS}\cdot\Delta t}) \quad (6)$$

where $[H_2O_2]_{SS,segment}$ represents the steady-state concentration of H_2O_2 in the respective irradiation segment. This value was computed by employing the approximating power functions together with the calculated average dose rate of each irradiation segment (Supporting Information, Table S1 and Table S2). $[H_2O_2]_{ti-1}$ is the H_2O_2 concentration at the previous time t_{i-1}, Δt is the time interval between t_i and t_{i-1} (100 s) and k_{SS} represents the time constant in Hz (a more in-depth description is given below). The difference in H_2 levels for the steady-state approximation ($\Delta[H_{2,SS}]$) is computed by the same equation after replacing $[H_2O_2]_{SS,segment}$ with the steady-state concentration of H_2 for the respective irradiation segment, that is, $[H_2]_{SS,segment}$ (Supporting Information, Table S2), and using the preceding H_2 concentration $[H_2]_{ti-1}$.

The time constant, k_{SS}, was introduced as a free variable to consider the limited residence time in the beam strike volume and the consequential time delay in the approximation of steady-state concentrations within the system's water. The Microsoft Excel Solver plug-in was used to find a value for k_{SS} that minimizes the χ^2 difference between the measured values of H_2 and H_2O_2 and the values produced by eq 5 at these times.

For the G_{eff} model the difference in H_2O_2 levels ($\Delta[H_2O_{2,Geff}]$) in one time step is estimated by eq 7:

$$\Delta[H_2O_{2_{G_{eff}}}] = \frac{P(t_i)G_{eff}\Delta t \times 10^4}{N_A \times V_{water}} - [H_2O_2]_{t_{i-1}}(1 - e^{-k_{KLC}\cdot\Delta t}) \quad (7)$$

where $P(t_i)$ represents the power of the $^1H^+$ beam at time t_i (eV/s), G_{eff} is the effective H_2O_2 yield (molecules/100 eV), and N_A is the Avogadro constant (6.022×10^{23} particles/mol). $[H_2O_2]_{t-1}$ represents the hydrogen peroxide concentration at the preceding time t_{i-1}, and Δt is the time interval between t_i and t_{i-1} where 100 s was used. The total water volume (V_{water}) is 36 L and k_{KLC} is the hydrogen peroxide decomposition rate of the catalytic converter (3.34×10^{-5} s^{-1}).[24]

Equation 8 was used to approximate the difference in H_2 levels for the G_{eff} model ($\Delta[H_{2,Geff}]$):

$$\Delta[H_{2_{Geff}}] = \frac{P(t_i)G_{eff}\Delta t \times 10^4}{N_A} - \frac{[H_{2,water}]_{t_{i-1}}\beta_1\Delta t}{V_{water}} + \frac{[H_{2,headspace}]_{t_{i-1}}\beta_1 K_H RT\Delta t \times 10^{-6}}{V_{headspace}} \quad (8)$$

The amount of H_2 in the headspace is represented by $[H_2]_{headspace}$, and the factor β_1 describes the kinetics of the exchange process ($\beta_1 \sim 0.05$ L/s). R is the ideal gas constant (8.21×10^{-3} L·atm/K·mol), K_H is Henry's law constant for H_2 (780 μM/atm), and T is the bulk water temperature (~298 K). A volume of ~10 L was used for the headspace ($V_{headspace}$).

3. RESULTS AND DISCUSSION

To demonstrate the validity of the developed model, the γ-radiolysis simulation with a closed 20 mL water container, which was previously described by Pastina et al., was repeated, and the results were compared.[19] Following the development of the relevant water decomposition products over the irradiation time, the computed concentration levels are largely in agreement with the previously published data (see Figure 1 in Pastina et al.[19]). However, the computed steady-state concentrations are moderately lower, which could be due to the updated rate constant data used in our simulation (Table 2). In this way, the suitability of the fundamental code setup

https://doi.org/10.1021/acsomega.2c03540
ACS Omega 2022, 7, 25860−25873

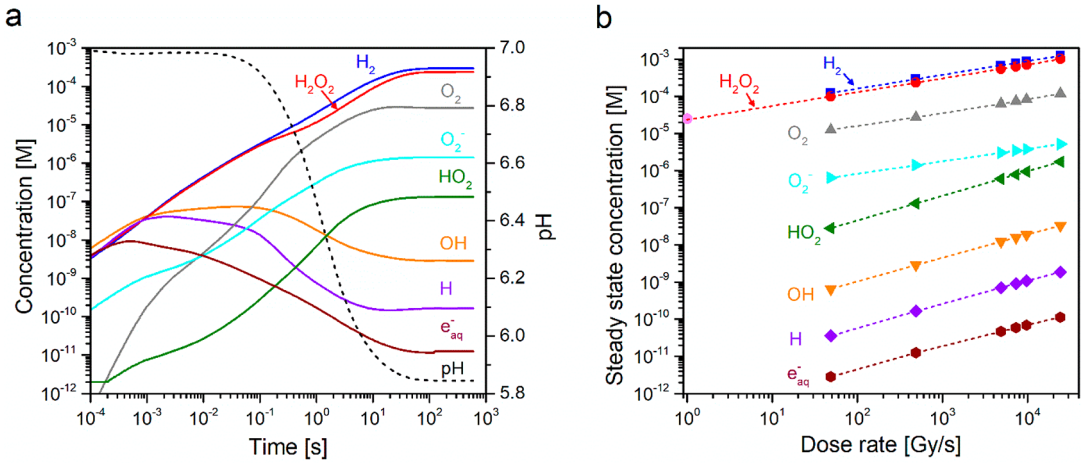

Figure 2. (a) Temporal development of relevant water decomposition products in 20 mL of pure water during the irradiation (600 s), simulated with 9.7 MeV $^1H^+$ at a beam current of 1 μA. The pH of the irradiated water is displayed on the secondary *y*-axes. (b) The computed steady-state concentrations of several molecular, radical, and ionic radiolysis products (H_2, H_2O_2, O_2, O_2^-, HO_2, OH, H, e^-_{aq}) as a function of dose rate in pure water. The dashed lines are the power function fits to the data. The measured steady-state concentration of H_2O_2 for 10 MeV $^1H^+$, published by Pastina et al.[19] (pink data point), is in line with the simulated data points (red data points).

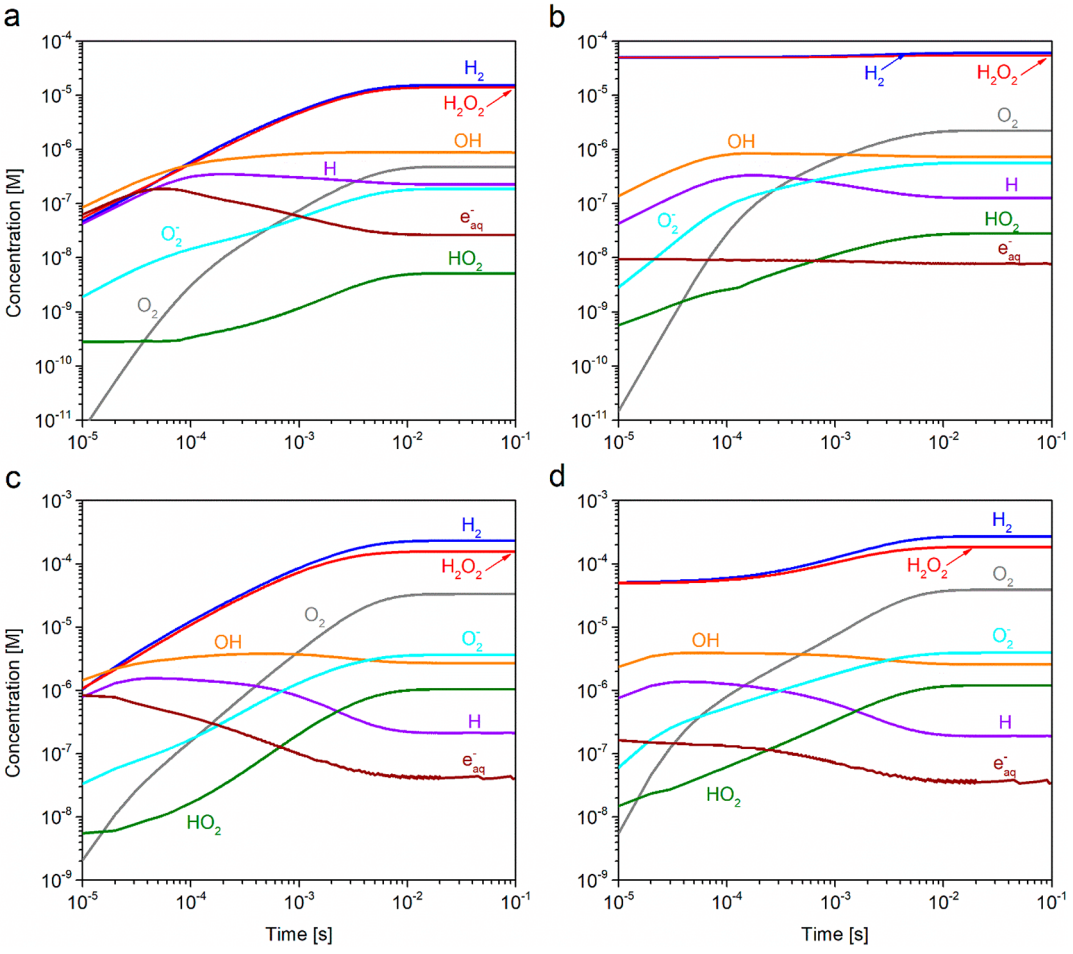

Figure 3. Temporal development of relevant water decomposition products in the beam strike volume of the flowing-water target, irradiated with proton beam intensities of (a, b) 1 μA and (c, d) 20 μA . The water that is initially present as well as the in-flowing water contained (a, c) 0 μM of the stable molecular species H_2, H_2O_2, and O_2 and (b, d) 50 μM H_2 and H_2O_2, respectively.

was confirmed and formed the basis for performing further experiments with protons.

3.1. Proton Irradiation of a Closed Container. In analogy to the gamma-ray irradiation of a closed 20 mL water container, similar computations were performed with 9.7 MeV protons. In Figure 2 a the development of relevant molecular, ionic, and radical species during the irradiation with a beam current of 1 μA is displayed. Initial levels of H_2, H_2O_2, OH, H,

https://doi.org/10.1021/acsomega.2c03540
ACS Omega 2022, 7, 25860−25873

and e^-_{aq} range between 10^{-9} and 10^{-8} M, whereas the levels of O_2 and O_2^- are considerably lower. The formation of HO_2 is observed with some time delay and exceeds 10^{-11} M only after ∼6 ms. Throughout the irradiation, the concentrations of H_2, H_2O_2, O_2, O_2^-, and HO_2 show an increasing trend, while the levels of OH, H, and e^-_{aq} are decreasing. H^+ ions are a primary water radiolysis product and their generation by the incoming proton beam results in a local decrease of the pH during the irradiation.[30] To appropriately approximate the radiolysis chemistry in our simulation, the ratio between protonated and deprotonated species of all conjugate acid−base pairs is allowed to adjust with the prevailing pH. Further, the simulation considers a complete dissolution of all radiolytically produced gases. This is because the pressure within the closed container increases relative to the formed H_2 and O_2 and, in agreement with Henry's law, the solubility of a gas is directly proportional to its partial pressure above the liquid.

After an irradiation time of ∼100 s, the concentrations of all radiolytic products remain essentially unchanged. Such a scenario is referred to as a steady state and is defined by an equal rate of formation and decomposition. For most species the main production path is the primary radiolysis process, while the removal is typically mediated by reactions between molecules with radicals and ions.[20,21] Equation 9 describes the steady-state concentration of the primary radiolysis product A ($[A]_{SS}$), where the production is determined by the dose rate (D_R) and the respective G value (G_A), and the decomposition is given by the rate constant (k_{A+B}) for the reaction of A with chemical species B.

$$[A]_{SS} = \frac{G_A \times D_R}{\sum_B k_{A+B} \times [B]} \tag{9}$$

The concentrations of other radiolysis products, which also depend on the dose rate, are included in the denominator, resulting in an approximate square-root dependency of the steady-state concentration on the dose rate (Supporting Information, Table S1). The exponents for the molecular species are slightly lower than 0.5, while the ones of radical species are marginally higher. The computed steady-state concentrations of several radiolysis products as a function of the dose rate are visualized in Figure 2b. The steady-state concentrations of hydrogen peroxide, estimated with this approximation, are in line with the experimentally obtained data from Pastina et al.[19] (Figure 2b, pink data point). A similar behavior for the steady-state concentrations of γ-radiolysis products was described experimentally as well as by model calculations.[20,21,26,30] In comparison to γ-rays, the absolute steady-state concentrations of the molecular species are considerably higher for protons, while the radical quantities are diminished. Such behavior is expected from the absolute values of the radiolytic yields for protons and gamma-rays and can be explained by the different LETs of the radiation (a more in-depth explanation is given in the following section). Equilibrium conditions are approached rapidly for low-LET radiation, while at increased LET the concentrations of molecular species increase nearly linearly with time, and steady-state conditions are reached much more slowly.[19,21,30] However, with high-LET radiation, water molecules will be decomposed continuously, and the approximation of a steady state is not expected.[13,22]

3.2. Radiolysis Reactions in the Proton-Irradiated Flowing-Water Target. The temporal development of relevant radical, ionic, and molecular products (H_2, H_2O_2, O_2, OH, e^-_{aq}, O_2^-, HO_2, H) inside the beam strike volume of the flowing-water target was computed for four different scenarios and is exemplified in Figure 3. The simulations were set up in a way that the entire volume was either filled with pure water or a solution of 50 μM H_2 and H_2O_2 prior to the onset of irradiation, and was also supplied with the same fluid throughout the beam irradiation (in the following referred to as "baseline" and "in-flowing solution" concentrations). The concentration levels of the radiolytic species were followed for 100 ms; however, a steady-state concentration was already approximated after an irradiation time of ∼6 ms. This is unlike the observations for the closed container (Figure 2a), where an equilibrium was achieved only after prolonged irradiation times. In the dynamics of the flowing-water target, the establishment of a dynamic equilibrium is determined by the removal rate, which depends on the outgoing water flow. At the set flow rate of 41.7 mL/s, the entire beam strike volume is replaced by fresh water after ∼3.4 ms which can be considered as the onset of the dynamic equilibrium.

After an irradiation time of ∼20 ms, an apparent steady state was established, and the resulting levels of H_2, H_2O_2, and O_2 were used to compute the effective yields, also denoted as effective G values, G_{eff}. The escape yields (or "G values") of radiolytic products are defined as the yield at the end of the nonhomogeneous track expansion before any homogeneous reactions occur. The calculated effective G values for H_2 and H_2O_2 for pure water and solutions encompassing 50 μM H_2 and H_2O_2 (scenarios represented in Figure 3) are displayed in the first two columns of Table 3. In comparison to the published escape yields for H_2 and H_2O_2, amounting to 0.64 and 0.74 molecules/100 eV,[19] the G_{eff} values were noticeably diminished. A similar trend could be identified for the effective yields which were computed for a wide range of beam currents and H_2, H_2O_2, and O_2 concentrations (Supporting Information, Table S3a−d). However, throughout all these different scenarios, the material balance between the number of H and

Table 3. Effective Yields, G_{eff}, the Percentage Metric for Total Yield Suppression, S_{total}, the Percentage Metric for Yield Suppression by Allen Cycle rxn, S_{Allen}, and the Percentage Metric for Yield Suppression by H_2O_2-Mediating rxn, $S_{H2O2rxn}$, of Different Solutions Computed for Low and High (1 and 20 μA) Beam Intensity Irradiations of the Flowing-Water Target

	G_{eff} (molecules/100 eV)		S_{total} (%)		S_{Allen} (%)		$S_{H2O2rxn}$ (%)	
	1 μA	20 μA	1 μA	20 μA	1 μA	20 μA	1 μA	20 μA
for 0 μM H_2, H_2O_2								
H_2	0.63	0.48	0.2	25	2	26		
H_2O_2	0.57	0.33	23	56	3	12	26	58
for 50 μM H_2								
H_2	0.52	0.45	19	29	20	30		
H_2O_2	0.49	0.32	34	57	17	14	37	59
for 50 μM H_2O_2								
H_2	0.60	0.49	7	24	9	25		
H_2O_2	0.22	0.29	70	61	10	13	71	63
for 50 μM H_2, H_2O_2								
H_2	0.42	0.46	34	28	35	29		
H_2O_2	0.19	0.28	75	62	23	15	75	64

https://doi.org/10.1021/acsomega.2c03540
ACS Omega 2022, 7, 25860−25873

O atoms of all created radiolytic species equals the net water decomposition. (A more in-depth explanation is given in the Supporting Information, "Net water decomposition".) Similar discrepancies between the measured H_2 and H_2O_2 levels and the escape yield-based predictions were observed earlier.[19,23,31] Following the end of the nonhomogeneous phase, the system transitions toward a homogeneous regime. There the regulatory effect of the chemical reactions is of increasing significance, particularly at elevated radical concentrations. The radiation's LET determines the structure of the tracks and thereby directly impacts the quantity of radicals. Dispersed ionization events at low LET result in few intratrack reactions and a significant number of radicals can escape into the bulk solution. At high-LET conditions, single ionization events coalesce, leading to increased radical densities which enhances the probability to react with each other, and consequently, more molecular products are disseminated.[16,19,23,32,33] Pastina et al. demonstrated that homogeneous reactions play a significant role for 10 MeV protons, which are characterized by a moderate LET value, and influence the observed levels of H_2 and H_2O_2.[19] (A more in-depth explanation of this observation is given in the next paragraph.) A similar suppressive effect on the H_2 and H_2O_2 concentrations can be assumed for the irradiations of our flowing-water target with 9.7 MeV protons.

By consecutively suppressing individual chemical reactions, it became possible to identify the ones which strongly influence the levels of H_2 and H_2O_2. A mechanism known as the "Allen cycle" is an important mediator for the concentrations of H_2 and H_2O_2 and starts with the reaction of hydrogen with hydroxyl radicals. Subsequently, the formed hydrogen atoms react with hydrogen peroxide, forming hydroxyl radicals and water.[34] The relevant reactions are given in Table 2, rxn 35 and 43. Within this chain mechanism, an effective elimination of H_2 and H_2O_2 is facilitated. A crucial precondition for the Allen cycle is the presence of radicals, particularly of OH and H. A LET of about 20 eV/nm is considered as a threshold below which adequate levels of radicals can escape from the ionization tracks to support the recombination reactions. With a LET of 12 eV/nm, the 9.7 MeV protons of the current experiment are below this threshold LET and can therefore contribute toward an effective annihilation of H_2 and H_2O_2.[19,23,26,35] An inhibiting effect was seen at excessive O_2 concentrations, which was also reported in previous studies.[19]

In our flowing-water target, the quantity of hydrogen is mainly regulated by the Allen cycle. However, a continuous reaction cycle can only be established when H_2 and H_2O_2 are present in sufficient amounts. This is the case at increased concentration levels or at enhanced beam intensities, which in turn generate higher levels of radiolytic species. When none of these conditions are given, as in the case of pure water irradiated with a low beam current (Table 3), the effective hydrogen yield (0.63 molecules H_2/100 eV) is similar to the literature escape yield (0.64 molecules H_2/100 eV).[19] However, when exposing the same solution to higher beam intensities, suppression of the effective H_2 yield by 25% was achieved. (A more in-depth explanation about the metrics used to characterize the yield suppression is given in the Material and Methods section.) The irradiation of solutions containing either 50 μM H_2 or 50 μM H_2O_2 yielded similar results, whereas a beam current-independent suppression of 34 and 28% was observed when both components were present. The good agreement for all different solutions between S_{total} and S_{Allen} for the H_2 data supports an almost exclusive Allen cycle-mediated H_2 regulation.

In the case of hydrogen peroxide, the discrepancies between S_{total} in comparison to S_{Allen} suggest a considerable influence of other decomposition reactions. The interactions of peroxide with OH radicals (rxn 44) and hydrated electrons (rxn 19) were identified as the main alternative annihilation pathways. Similar radiolytic reaction channels for hydrogen peroxide were reported by previous studies.[19,23,26,31] The increased complexity of the hydrogen peroxide reaction scheme is reflected by the larger extent of total H_2O_2 suppression in comparison to the effects observed for hydrogen. For pure H_2O_2 solutions or mixtures of H_2O_2 and H_2, a decrease of 61−75% was seen, whereas a lower, and beam current-sensitive effect was observed for pure water and solutions containing only H_2. When the latter solution compositions were irradiated with low beam currents, the reaction of hydrogen peroxide with OH radicals (rxn 44) was shown to be hampered, which could be due to limited interactions between radicals and molecules. The efficiency of the H_2O_2 decomposition with hydrated electrons (rxn 19) was not affected by different beam intensities. With $S_{H2O2\ rxn}$ the influence of the main peroxide decomposition (rxn 19, 35, 43, 44) and formation reactions (rxn 40) are considered. The good agreement with the total H_2O_2 yield suppression underlines the importance of all these reactions in the H_2O_2 reaction pathway. For gamma-ray and proton irradiations with LETs below the 20 eV/nm threshold, similar reductions of the H_2O_2 concentration, also in the absence of additional H_2, were reported.[19,23]

The formation of H_2 and H_2O_2 occurs mainly within the track, which is usually followed by an outward diffusion into the bulk water. Within the homogeneous regime, the chemistry is mainly determined by secondary reactions of radicals with stable molecular species.[23,31] The resulting yield attenuation of molecular products is described in detail above. Interactions between radicals play an inferior role, and as such, only a slight increase in the quantities of molecular products is observed.[19] In the case of hydrogen, the combination of H atoms (rxn 33), as well as the reaction of H atoms with hydrated electrons (rxn 24), has a moderately enhancing effect on the H_2 levels. The latter reaction plays a limited role and is only relevant at elevated molecular hydrogen concentrations. The combination of OH radicals (rxn 40) is known to be the main intratrack process leading to the formation of hydrogen peroxide.[23,31,32] However, in the homogeneous domain rxn 40 is only of minor significance and limited to low H_2O_2 concentrations, particularly at low beam currents.

The observations of the hydrogen and hydrogen peroxide yields suggest that at elevated beam currents, the attenuation of both species depends only marginally on the solution composition. At FRIB, heavy-ion beams of high intensity will be stopped in the water-traversed beam blocker drum.[1] From the studies with our flowing-water target, suppressed effective H_2 and H_2O_2 yields, in comparison to the literature escape yields, can be expected at FRIB.

3.3. Proton Beam-Induced Radiolysis of the System's Water. The "Design of Experiments" feature of the statistical software Minitab was employed to minimize the computational effort to determine the functional dependencies of the effective G values of H_2, H_2O_2, and O_2 on their respective concentrations as well as on the beam current. Such a systematic approach allows finding the cause-and-effect relationships by performing the least possible number of

https://doi.org/10.1021/acsomega.2c03540
ACS Omega 2022, 7, 25860−25873

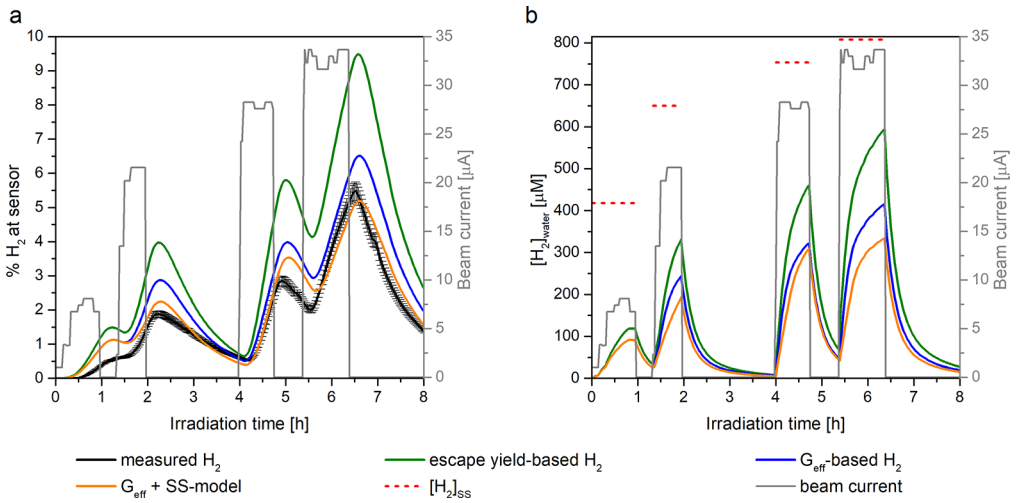

Figure 4. (a) The measured % H_2 at the sensor (black line) is approximated by different estimations: The escape yield- and the G_{eff}-based models (green and blue line) predict higher H_2 levels, while the G_{eff} + SS-model suggests a reasonable approximation (orange line). (b) The steady-state concentrations of H_2 in the system's water are calculated for each irradiation segment (red dashed lines) and are an integral part of the G_{eff} + SS-based calculation (orange line). The corresponding beam current (gray line) is outlined on the secondary *y*-axes for both panels a and b.

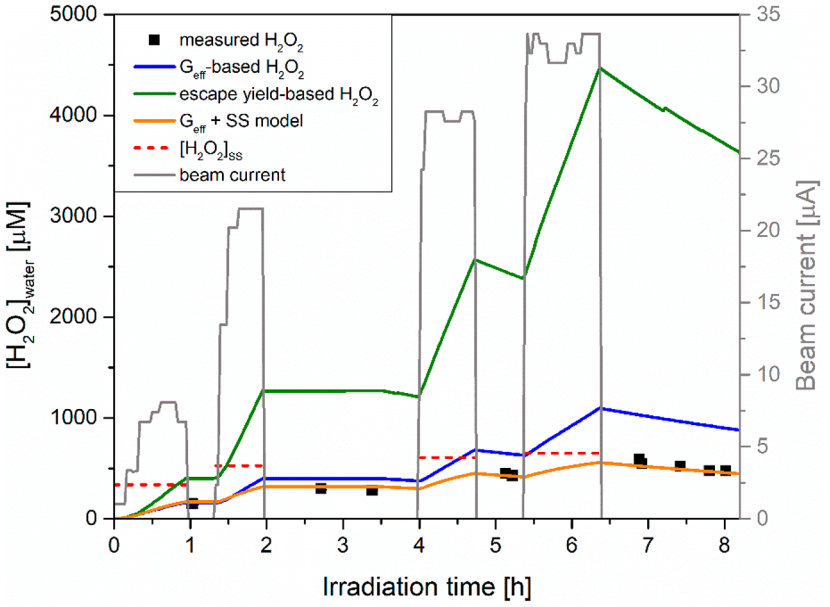

Figure 5. Escape yield- and the G_{eff}-based prediction (green and blue line) overestimate the measured H_2O_2 concentrations (black squares). However, with the G_{eff} + SS-based estimation (orange line) an adequate approximation could be realized. The steady-state concentrations of H_2O_2 for each irradiation segment are outlined by the red dashed lines.

experimental runs. To approximate the dependency of the four input variables (H_2, H_2O_2, and O_2 concentration, beam current) and the computed G_{eff} values of the corresponding molecular species by an empirical model, a careful selection of the input ranges is required. Here the beam current was adopted as the decisive parameter and the entire range was divided into four segments. In comparison to other input factors, the beam current was regulated, and was therefore less susceptible to variations. The so-obtained polynomial equations, including the coefficients and terms of the functional dependency analysis, are given in the Supporting Information, Table S5a–d.

By applying the determined regression equations for G_{eff}(H_2, H_2O_2, O_2), the concentration levels of all molecular species could be mapped over the entire irradiation time, and the results are displayed in Figures 4a, 5, and 6. In the case of hydrogen (Figure 4a), the effective yield prediction suggests about 1.4-times higher H_2 concentration than observed throughout the entire irradiation. However, with the escape yield-based calculation (assuming a constant G value of 0.64 molecules H_2/100 eV[19]), the percentage of H_2 was estimated to be about 2-times higher. The H_2 data acquired within the first irradiation segment was not included in these considerations, since the sensor was not yet adequately equilibrated to the measurement conditions.

At elevated beam currents, the discrepancies between the measured and G_{eff}-predicted hydrogen peroxide levels increased (Figure 5). For the end of the first irradiation period, the prediction suggests 1.1-times higher H_2O_2 levels than observed, which developed to a 1.9-fold increase after

https://doi.org/10.1021/acsomega.2c03540
ACS Omega 2022, 7, 25860−25873

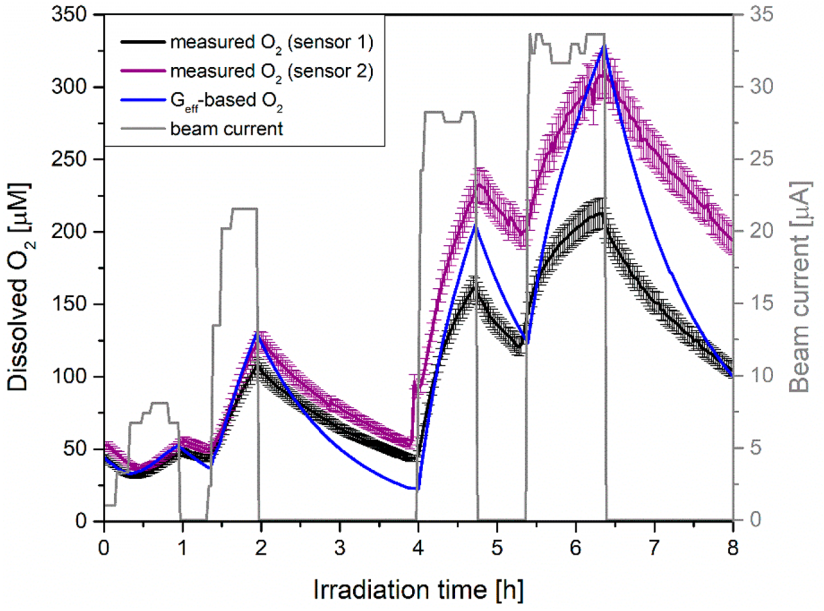

Figure 6. Dissolved oxygen levels were assessed before (sensor 1) and after (sensor 2) the water was passed over the catalytic converter unit (black and purple lines). The O_2 levels of the system's water, which were assessed by sensor 1, were approximated with the G_{eff}-based estimation (blue line).

6.4 h. However, with the escape yield model (assuming a constant G value of 0.74 H_2O_2 molecules/100 eV[19]), a maximum of 4.5 mM H_2O_2 was estimated, which is 7.5-times greater than the measured concentrations.

The dissolved oxygen content in the water was assessed with two sensors (sensors 1 and 2), placed before and after the catalytic hydrogen peroxide decomposition unit. The initially comparable sensor readings diverged when the water was passed over the catalytic unit with the onset of the third irradiation period (Figure 6). The exact stoichiometric relationship between H_2O_2 decomposition and O_2 discharge was already discussed by Abel et al. and is also considered in the here performed G_{eff}-based calculation.[24] Similar to the estimated hydrogen peroxide levels, increasing discrepancies between the oxygen levels measured by sensor 1 and the computed predictions became discernible. For the end of the last irradiation period, the computed values were 1.5-times higher than observed; however, only a maximum 1.2-fold increase was noticeable in all previous irradiation segments. Since molecular oxygen is not a primary water decomposition product, no escape yield-based prediction was performed. The G_{eff}-based calculation considers the oxygen formation by secondary reactions within the homogeneous phase. It needs to be mentioned that additional O_2 was generated by the catalytic H_2O_2 decomposition, which renders the relatively low oxygen levels susceptible to external influences, such as small variations in the converter's decomposition rate or the deaeration rate. With this experimental setup it is not possible to clearly evaluate any deviations between the estimated and measured oxygen levels, thus no further analytical estimations were attempted.

In general, the G_{eff}-based calculation allowed a reasonable approximation of the H_2 and H_2O_2 trends, however, the predictions overestimated the observed concentrations. The effective yield computation takes into account the influence on the literature escape yields by the homogeneous chemical reactions, the geometry of the beam strike volume, and the continuous water flow. The latter determines the removal rate of radiolytic species and facilitates the rapid establishment of an apparent steady state inside the beam strike volume. Even though radiolysis phenomena have been extensively described in the literature, most experiments involved the irradiation of an enclosed volume of less than 100 mL. Under such conditions, a homogeneous distribution of the formed radiolysis products and the water molecules can be assumed. By exposing a definite volume to constant low-LET radiation over prolonged time periods, a steady state will establish and determine the concentrations of all radiolytic species.[19−21,23,26] In our case, the setup encompassed a small, beam irradiated chamber (0.14 mL) connected to a nonirradiated, large water volume (~36 L). While steady-state conditions are approximated rapidly in limited volumes, extensive irradiation times would be necessary to deliver the required dose to the entire system's water. However, since the total amount of radiation was deposited only into the beam strike volume, a considerably lower dose and shorter irradiation time would be necessary to approach a local steady state. Based on these assumptions, the steady-state concentrations of H_2 and H_2O_2 were estimated for each irradiation segment by applying the previously outlined equations, which characterize the steady-state concentrations as a function of dose rate (Supporting Information, Table S1). With the slight beam current variations in each irradiation segment, the calculation with the average dose rate was regarded as adequate (Supporting Information, Table S2). Under uniform irradiation conditions, the necessary time to approach steady-state conditions is determined by the applied dose rate. However, in our system the time structure is additionally affected by the limited residence time inside the beam strike volume. Based on these conditions, a model was developed that considers the G_{eff}-mediated formation as well as the attenuating effect of the established steady state. To estimate the rate of the steady-state approximation, a time constant, k_{SS}, was introduced. This is a free variable, which was fitted to 2.64×10^{-4} s^{-1} at the minimized χ^2 difference

https://doi.org/10.1021/acsomega.2c03540
ACS Omega 2022, 7, 25860−25873

between the measured and estimated H_2 and H_2O_2 concentrations. With the G_{eff} + SS-based calculation, the amount of H_2 in the system's water was calculated (Figure 4b) and converted to the percentage H_2 at the sensor to allow a comparison with the measured data (Figure 4a). In this way, a reasonable approximation became possible, though the levels after the third irradiation segment are moderately overestimated. The observed discrepancies might be due to the removal of H_2 from the water and slight variations in the flow of the purge gas stream. The G_{eff} + SS-model also allowed an adequate estimation of the measured H_2O_2 levels over the entire irradiation time (Figure 5). It needs to be emphasized, that this model requires a fitted time constant k_{SS}, which, so far, is not confirmed by experimental measurements. The time constant is primarily influenced by the conditions of the system, such as the flow rate. However, since k_{SS} allows the extrapolation of a scenario where the water flow rate is set to zero (i.e., irradiation of a closed small-volume container) toward a flowing-water system with a connected large, nonirradiated volume, it includes any deviations related to such an estimation. Even though the establishment of a steady state in the entire system's water is only based on simulations, the resulting model can explain our observations during the $^1H^+$ beam experiment. In the anticipated experimental confirmation, prolonged irradiation times at a constant dose rate are foreseen.

In this study we propose the establishment of a steady state for particle radiation with limited LET, such as 9.7 MeV protons, for an open, large-size system. This can be seen as an extension of previous studies, in which the approximation of a steady state has only been described for irradiations of small water volumes with low to moderate LET radiation.[19−21,23,26,30] The here described steady state-based calculation can be directly translated toward FRIB conditions and aid in estimating the expected molecular product levels generated by ion beams of limited LET. However, at FRIB predominantly high-intensity, heavy-ion beams will be stopped in the beam dump, inducing various nuclear reactions that result in a range of diverse secondary, and sometimes even tertiary, beam fragments. Next to the generation of beam products, high-energy neutrons and γ-rays are expected as well,[36,37] which will contribute to the radiolysis of water molecules. The resulting radiation field will be determined by the ratio of the different radiation types, however, for most primary heavy-ion beams a strong high-LET component can be expected. Radiation characterized by a high LET contributes to a continuous decomposition of water molecules, while the convergence to steady-state concentrations of molecular products is not expected.[13,22] The comparable setup of the FRIB beam dump to our flowing-water target would suggest an effective yield-based H_2, H_2O_2, and O_2 formation, which is still considerably diminished in comparison to an escape yield-mediated production.

Even when considering an effective yield-based formation of radiolytic species in FRIB's isotope harvesting beam dump, elevated molecular products can be expected in the system's water. Such levels can render modest equipment wear possible, and influence the chemical behavior of radionuclides with sensitive trace-level aqueous chemistry, which could complicate the anticipated isotope harvesting efforts. A catalytic recombination unit is foreseen to keep the amount of radiolytic hydrogen and oxygen within limits. The large surface area of the water system's stainless-steel pipes was previously assumed to effectively decompose hydrogen peroxide. However, the exposure of stainless-steel surfaces to large quantities of H_2O_2 has been shown to reduce the rate of degradation, resulting in increased H_2O_2 concentrations within the system's water.[4]

The addition of H_2 to the primary coolant water of pressurized water reactors has been effective in preventing the buildup of oxidizing species. In these systems, ^{10}B is added to the water as moderator and represents a source of high- LET ^4He and ^7Li particles, while the water is also exposed to γ-radiation and fast neutrons. With low-LET radiation excessive amounts of radicals are generated, which support the recombination of hydrogen peroxide in a hydrogen-rich environment.[38] However, the extent of water decomposition is strongly dependent on the local ratio between high- and low-LET radiation. In pure alpha beam irradiations, a decrease of the steady-state concentrations could only be observed when alpha particles of limited LET were applied, while high-LET alpha beams created an unchanged, almost linear increase of hydrogen peroxide levels.[19,39] The radiation field created by FRIB's primary heavy-ion beams, when impinging onto the beam dump, is expected to entail a considerable amount of high-LET radiation. For every beam type and energy, it is necessary to determine whether the low-LET component can maintain a sufficient level of radical species to realize an effective recombination at elevated hydrogen levels. An alternative option to reduce the levels of hydrogen peroxide could be based on catalytic decomposition, like the catalytic converter unit in our harvesting system. This method would allow an effective peroxide decomposition independent from the prevalent radical concentrations. However, to allow a more confident prediction, a translation of the simulation model to include the dimensions and flow dynamics of the rotating FRIB beam dump would be necessary. The here established kinetic modeling of the homogeneous radiolysis phase of the flowing-water target will contribute toward the development of an adequate simulation for the conditions at FRIB.

4. CONCLUSIONS

In the high-intensity proton irradiation of our isotope harvesting system, lower levels of radiolytic hydrogen and hydrogen peroxide were observed than expected. While a suppression of the escape yield-based formation is assumed for closed, limited volumes, fewer interactions between radiolytic species are expected to occur in open, large-size systems like ours. With the developed simulation model, the noticeable influence of homogeneous interactions within the dynamics of the flowing-water target could be estimated. The decreased effective yields showed a dependency on the prevailing concentrations of molecular hydrogen, oxygen, and hydrogen peroxide as well as on the applied beam current. However, the experimental measurements could only be approximated by a model that additionally considers the establishment of a steady state. Such an effect, previously only described for enclosed systems subjected to low-LET radiation, is made possible by the small beam strike volume connected to the large water tank via mass transfer. However, for the heavy-ion beams at FRIB an effective yield-based formation is expected. The here developed simulation model provides a reasonable basis for a translation toward the conditions at FRIB and thereby aid in estimating the levels of generated molecular products.

https://doi.org/10.1021/acsomega.2c03540
ACS Omega 2022, 7, 25860−25873

■ ASSOCIATED CONTENT

Supporting Information

The Supporting Information is available free of charge at https://pubs.acs.org/doi/10.1021/acsomega.2c03540.

Additional details about the computation of the H_2, H_2O_2, and O_2 levels in the isotope harvesting system, power functions for estimating the steady-state concentrations, tables of computed effective G values and steady-state concentrations of H_2 and H_2O_2, schematics of the isotope harvesting setup and the flowing-water target (PDF)

■ AUTHOR INFORMATION

Corresponding Author

Katharina A. Domnanich − *Department of Chemistry, Michigan State University, East Lansing, Michigan 48824, United States; National Superconducting Cyclotron Laboratory and Facility for Rare Isotope Beams, Michigan State University, East Lansing, Michigan 48824, United States;* orcid.org/0000-0002-3777-3192; Phone: +1-517-908-7000; Email: domnanic@frib.msu.edu

Author

Gregory W. Severin − *Department of Chemistry, Michigan State University, East Lansing, Michigan 48824, United States; National Superconducting Cyclotron Laboratory and Facility for Rare Isotope Beams, Michigan State University, East Lansing, Michigan 48824, United States*

Complete contact information is available at: https://pubs.acs.org/10.1021/acsomega.2c03540

Notes

The authors declare no competing financial interest.

■ ACKNOWLEDGMENTS

This research is supported under award DE-SC0021220 by the U.S. Department of Energy Isotope Program, managed by the Office of Isotope R&D and Production. The authors would like to thank Prof. Jonathan Engle and Todd Barnhardt for providing and tuning the proton beam. Additionally, we would like to acknowledge the support of Morgan Kalman and Wes Walker for setting up the isotope harvesting system. We would also like to thank Dr. Paige Abel, Dr. Frederique Pellemoine, and Prof. Wolfgang Mittig for the insightful discussions.

■ REFERENCES

(1) Hausmann, M.; Aaron, A. M.; Amthor, A. M.; Avilov, M.; Bandura, L.; Bennett, R.; Bollen, G.; Borden, T.; Burgess, T. W.; Chouhan, S. S.; Graves, V. B.; Mittig, W.; Morrissey, D. J.; Pellemoine, F.; Portillo, M.; Ronningen, R. M.; Schein, M.; Sherrill, B. M.; Zeller, A. Design of the advanced Rare Isotope Separator ARIS at FRIB. *Nucl. Instruments Methods Phys. Res. Sect. B Beam Interact. with Mater. Atoms* **2013**, *317* (B), 349−353.

(2) Abel, E. P.; Avilov, M.; Ayres, V.; Birnbaum, E.; Bollen, G.; Bonito, G.; Bredeweg, T.; Clause, H.; Couture, A.; DeVore, J.; Dietrich, M.; Ellison, P.; Engle, J.; Ferrieri, R.; Fitzsimmons, J.; Friedman, M.; Georgobiani, D.; Graves, S.; Greene, J.; Lapi, S.; Loveless, C. S.; Mantica, P.; Mastren, T.; Martinez-Gomez, C.; McGuinness, S.; Mittig, W.; Morrissey, D.; Peaslee, G.; Pellemoine, F.; Robertson, J. D.; Scielzo, N.; Scott, M.; Severin, G.; Shaughnessy, D.; Shusterman, J.; Singh, J.; Stoyer, M.; Sutherlin, L.; Visser, A.; Wilkinson, J. Isotope Harvesting at FRIB: Additional Opportunities for Scientific Discovery. *J. Phys. G* **2019**, *46*, 100501.

(3) Abel, E. P.; Clause, H. K.; Severin, G. W. Radiolysis and radionuclide production in a flowing-water target during fast $^{40}Ca^{20+}$ irradiation. *Appl. Radiat. Isot.* **2020**, *158*, 109049.

(4) Domnanich, K. A.; Abel, E. P.; Clause, H. K.; Kalman, C.; Walker, W.; Severin, G. W. An Isotope Harvesting Beam Blocker for the National Superconducting Cyclotron Laboratory. *Nucl. Instruments Methods Phys. Res. Sect. A Accel. Spectrometers, Detect. Assoc. Equip.* **2020**, *959*, 163526.

(5) Mastren, T.; Pen, A.; Loveless, S.; Marquez, B. V.; Bollinger, E.; Marois, B.; Hubley, N.; Brown, K.; Morrissey, D. J.; Peaslee, G. F.; Lapi, S. E. Harvesting ^{67}Cu from the Collection of a Secondary Beam Cocktail at the National Superconducting Cyclotron Laboratory. *Anal. Chem.* **2015**, *87* (20), 10323−10329.

(6) Mastren, T.; Pen, A.; Peaslee, G. F.; Wozniak, N.; Loveless, S.; Essenmacher, S.; Sobotka, L. G.; Morrissey, D. J.; Lapi, S. E. Feasibility of isotope harvesting at a projectile fragmentation facility: ^{67}Cu. *Sci. Rep.* **2014**, *4*, 1−6.

(7) Loveless, C. S.; Marois, B. E.; Ferran, S. J.; Wilkinson, J. T.; Sutherlin, L.; Severin, G.; Shusterman, J. A.; Scielzo, N. D.; Stoyer, M. A.; Morrissey, D. J.; Robertson, J. D.; Peaslee, G. F.; Lapi, S. E. Harvesting ^{48}V at the National Superconducting Cyclotron Laboratory. *Appl. Radiat. Isot.* **2020**, *157*, 109023.

(8) Pen, A.; Mastren, T.; Peaslee, G. F.; Petrasky, K.; Deyoung, P. A.; Morrissey, D. J.; Lapi, S. E. Design and construction of a water target system for harvesting radioisotopes at the National Superconducting Cyclotron Laboratory. *Nucl. Instruments Methods Phys. Res. Sect. A Accel. Spectrometers, Detect. Assoc. Equip.* **2014**, *747*, 62−68.

(9) Domnanich, K. A.; Vyas, C. K.; Abel, E. P.; Kalman, C.; Walker, W.; Severin, G. W. Harvesting ^{62}Zn from an aqueous cocktail at the NSCL. *New J. Chem.* **2020**, *44*, 20861−20870.

(10) Shusterman, J. A.; Scielzo, N. D.; Abel, E. P.; Clause, H. K.; Dronchi, N. D.; Frey, W. D.; Gharibyan, N.; Hart, J. A.; Loveless, C. S.; McGuinness, S. R.; Sutherlin, L. T.; Thomas, K. J.; Lapi, S. E.; Robertson, J. D.; Stoyer, M. A.; Norman, E. B.; Peaslee, G. F.; Severin, G. W.; Shaughnessy, D. A. Aqueous harvesting of ^{88}Zr at a radioactive-ion-beam facility for cross-section measurements. *Phys. Rev. C* **2021**, *103* (2), 1−12.

(11) Clause, H. K.; Domnanich, K. A.; Kleinfeldt, C.; Kalman, M.; Walker, W.; Vyas, C.; Abel, E. P.; Severin, G. W. Harvesting krypton isotopes from the off-gas of an irradiated water target to generate ^{76}Br and ^{77}Br. *Sci. Rep.* **2022**, *12* (1), 1−10.

(12) LaVerne, J. A.; Schuler, R. H. Track effects in the radiolysis of water: $HO_2\bullet$ production by 200−800-MeV carbon ions. *J. Phys. Chem.* **1992**, *96* (18), 7376−7378.

(13) Spinks, J. W. T.; Woods, R. R. *An Introduction to Radiation Chemistry*, 3rd ed.; John Wiley & Sons Ltd, 1964.

(14) Le Caër, S. Water radiolysis: Influence of oxide surfaces on H_2 production under ionizing radiation. *Water* **2011**, *3*, 235−253.

(15) Meesungnoen, J.; Jay-Gerin, J. P. High-LET radiolysis of liquid water with $^{1}H^{+}$, $^{4}He^{2+}$, $^{12}C^{6+}$, and $^{20}Ne^{9+}$ ions: Effects of multiple ionization. *J. Phys. Chem. A* **2005**, *109* (29), 6406−6419.

(16) Baldacchino, G.; Brun, E.; Denden, I.; Bouhadoun, S.; Roux, R.; Khodja, H.; Sicard-Roselli, C. Importance of radiolytic reactions during high-LET irradiation modalities: LET effect, role of O_2 and radiosensitization by nanoparticles. *Cancer Nanotechnol.* **2019**, *10* (1), 1−21.

(17) La Verne, J. A. Radiation chemical effects of heavy ions. In *Charged Particle and Photon Interactions with Matter*; Mozumder, A., Hatano, Y., Katsamura, Y., Eds.; CRC Press Inc., 2010; p 1064.

(18) Wasselin-Trupin, V.; Baldacchino, G.; Bouffard, S.; Hickel, B. Hydrogen peroxide yields in water radiolysis by high-energy ion beams at constant LET. *Radiat. Phys. Chem.* **2002**, *65* (1), 53−61.

(19) Pastina, B.; La Verne, J. A. Effect of molecular hydrogen on hydrogen peroxide in water radiolysis. *J. Phys. Chem. A* **2001**, *105* (40), 9316−9322.

(20) Joseph, J. M.; Choi, B. S.; Yakabuskie, P.; Wren, J. C. A combined experimental and model analysis on the effect of pH and

$O_{2(aq)}$ on γ-radiolytically produced H_2 and H_2O_2. *Radiat. Phys. Chem.* **2008**, *77* (9), 1009−1020.
(21) Wren, J. C. Steady-state radiolysis: Effects of dissolved additives. *ACS Symp. Ser.* **2010**, *1046*, 271−295.
(22) La Verne, J. A.; Schuler, R. H.; Ross, A. B.; Helman, W. P. Bibliographies on Radiation Chemistry. *Radiat. Phys. Chem.* **1981**, *12* (1), 5−20.
(23) Iwamatsu, K.; Sundin, S.; LaVerne, J. A. Hydrogen peroxide kinetics in water radiolysis. *Radiat. Phys. Chem.* **2018**, *145*, 207−212.
(24) Abel, E. P.; Domnanich, K.; Kalman, C.; Walker, W.; Engle, J. W.; Barnhart, T. E.; Severin, G. Durability test of a flowing-water target for isotope harvesting. *Nucl. Instruments Methods Phys. Res. Sect. B Beam Interact. with Mater. Atoms* **2020**, *478* (April), 34−45.
(25) McKee, D. W. Catalytic decomposition of hydrogen peroxide by metals and alloys of the platinum group. *J. Catal.* **1969**, *14* (4), 355−364.
(26) Ershov, B. G.; Gordeev, A. V. A model for radiolysis of water and aqueous solutions of H_2, H_2O_2 and O_2. *Radiat. Phys. Chem.* **2008**, *77* (8), 928−935.
(27) Ziegler, J. F.; Ziegler, M.D.; Biersack, J.P. SRIM - The Stopping Range of Ions in Matter. *Nuclear Instrum. Methods Phys. Res., Sect. B* **2010**, *268*, 1818.
(28) Elliot, A. J.; McCracken, D. R. Computer modelling of the radiolysis in an aqueous lithium salt blanket: Suppression of radiolysis by addition of hydrogen. *Fusion Eng. Des.* **1990**, *13* (1), 21−27.
(29) Elliot, A.; Bartels, D. The reaction set, rate constants and G-values for the simulation of the radiolysis of light water. *At. Energy Canada Ltd. Rep.* **2009**, 153−127160.
(30) Chatterjee, A.; Magee, J. L.; Dey, S. K. The role of homogeneous reactions in the radiolysis of water. *Radiat. Res.* **1983**, *96* (1), 1−19.
(31) Roth, O.; Laverne, J. A. Effect of pH on H_2O_2 production in the radiolysis of water. *J. Phys. Chem. A* **2011**, *115* (5), 700−708.
(32) Pastina, B.; LaVerne, J. A. Hydrogen peroxide production in the radiolysis of water with heavy ions. *J. Phys. Chem. A* **1999**, *103* (11), 1592−1597.
(33) LaVerne, J. A. Track Effects of Heavy Ions in Liquid Water. *Radiat. Res.* **2000**, *153* (5), 487−496.
(34) Allen, A. O.; Hochanadel, C. J.; Ghormley, J. A.; Davis, T. W. Decomposition of water and aqueous solutions under mixed fast neutron and gamma radiation. *J. Phys. Chem.* **1952**, *56* (5), 575−586.
(35) Hochanadel, C. J. Effects of cobalt γ-radiation on water and aqueous solutions. *J. Phys. Chem.* **1952**, *56* (5), 587−594.
(36) Gunzert-Marx, K.; Schardt, D.; Simon, R. S. Fast neutrons produced by nuclear fragmentation in treatment irradiations with 12C beam. *Radiat. Prot. Dosimetry* **2004**, *110* (1−4), 595−600.
(37) Le Foulher, F.; Bajard, M.; Chevallier, M.; Dauvergne, D.; Freud, N.; Henriquet, P.; Karkar, S.; Letang, J. M.; Lestand, L.; Plescak, R.; Ray, C.; Schardt, D.; Testa, E.; Testa, M. Monte Carlo Simulations of Prompt-Gamma. *IEEE Trans. Nucl. Sci.* **2010**, *57* (5), 2768−2772.
(38) Pastina, B.; Isabey, J.; Hickel, B. The influence of water chemistry on the radiolysis of the primary coolant water in pressurized water reactors. *J. Nucl. Mater.* **1999**, *264* (3), 309−318.
(39) Lertnaisat, P.; Katsumura, Y.; Mukai, S.; Umehara, R.; Shimizu, Y.; Suzuki, M. Simulation of the inhibition of water alpha-radiolysis via H_2 addition. *J. Nucl. Sci. Technol.* **2014**, *51* (9), 1087−1095.

https://doi.org/10.1021/acsomega.2c03540
ACS Omega 2022, 7, 25860−25873